water

MDPI

Article

Effect of the Surface Charge on the Adsorption Capacity of Chromium(VI) of Iron Oxide Magnetic Nanoparticles Prepared by Microwave-Assisted Synthesis

Alvaro Gallo-Cordova [1,*], María del Puerto Morales [1] and Eva Mazarío [1,2,*]

[1] Instituto de Ciencia de Materiales de Madrid, ICMM/CSIC, Sor Juana Inés de la Cruz 3, 28049 Madrid, Spain; puerto@icmm.csic.es

[2] Departamento de Química Física Aplicada, Facultad de Ciencias, Universidad Autónoma de Madrid, Francisco Tomás y Valiente 7, 28049 Madrid, Spain

* Correspondence: alvaro.gallo@csic.es (A.G.); eva.mazario@uam.es (E.M.)

Received: 15 October 2019; Accepted: 9 November 2019; Published: 13 November 2019

Abstract: Solid phase extraction using magnetic nanoparticles has represented a leap forward in terms of the improvement of water quality, preventing the contamination of industrial effluents from discharge in a more efficient and affordable way. In the present work, superparamagnetic iron oxide nanoparticles (MNP) with different surface charges are tested as nanosorbents for the removal of chromium(VI) in aqueous solution. Uniform magnetic nanoparticles (~12 nm) were synthesized by a microwave polyol-mediated method, and tetraethyl orthosilicate (TEOS) and (3-aminopropyl) triethoxysilane (APTES) were grafted onto their surface, providing a variation in the surface charge. The adsorptive process of chromium was evaluated as a function of the pH, the initial concentration of chromium and contact time. Kinetic studies were best described by a pseudo-second order model in all cases. TEOS@MNP barely removed the chromium from the media, while non-grafted particles and APTES@TEOS@MNP followed the Langmuir model, with maximum adsorption capacities of 15 and 35 mg_{Cr}/g, respectively. The chromium adsorption capacities abruptly increased when the surface became positively charged as the species coexisting at the experimental pH are negatively charged. Furthermore, these particles have proven to be highly efficient in water remediation due their 100% reusability after more than six consecutive adsorption/desorption cycles.

Keywords: water treatment; iron oxide nanoparticles; magnetic nanoparticles; magnetic harvesting; adsorption; chromium removal

1. Introduction

Many developed countries have decided to strengthen their environmental policies to minimize water pollution by regulating industrial activities regarding the discharge of hazardous chemicals, including heavy metals, as wastewater into the environment [1,2]. Heavy metals are considered persistent contaminants, and they cannot be easily degraded into harmless products [3]. Among others, Pb, As, Cd, Cu, Zn, Ni and Cr are the most hazardous. Chromium—in particular, in the two stable oxidation states Cr(III) and Cr(VI)—is one of the substances that poses a significant potential threat to human health due to its known toxicity in human exposure [4].

Common drinking water can be considered toxic when it contains more than 0.05 mg/L of Cr(VI), because this chromium state is found to be highly soluble and toxic. The chromates $HCrO^{4-}$ and $Cr_2O_7^{2-}$ have been discharged over the years by many industrial activities in the fields of petroleum refining, electroplating, metal coating and batteries, among others [1,5,6]. In a common

wastewater treatment process, the removal of these kind of compounds takes place through chemical and physical treatments using conventional methods such as coagulation and flocculation, membrane separation, oxidation, adsorption and ionic exchange [7,8]. Specifically, for chromium removal, different techniques are already applied at a large scale, such as bioremediation, reduction by electrochemical and biological methods and adsorption using nanosorbents such as carbon-based materials [9,10]. The last method—solid phase extraction—seems to be a very effective and affordable water treatment technique, and there have been numerous studies applied to different heavy metals [11–14].

The selection of the adsorbent is crucial when maximizing efficiencies in the removal process. It is very important that the material used as an adsorbent presents high adsorption capacities and allows a non-complex separation from the aqueous media [7,15]. In this sense, iron oxide magnetic nanoparticles (MNPs) take advantage of their easy separation by means of a magnet, and their reduced size provides a high specific surface area [16,17]. Magnetite nanoparticle sizes below 20 nm also present superparamagnetic behaviors, which is a reversible magnetic behavior that diminishes magnetic interactions and therefore aggregation, ensuring the easy reuse of the particles [18].

In the present work, uniform MNPs were prepared by microwave-assisted synthesis in polyol media [19]. One of the main advantages of this interesting approach is that microwave radiation allows a simple and controlled source of selective heating by ionic conduction and dipolar polarization that takes place at the same time for all of the reaction volume [20]. This is a highly reproducible method that has shown an increase in reaction yields and also an impressive reduction in the synthesis time compared to other conventional methods [21]. Magnetic nanoparticle sizes were tuned within the superparamagnetic limit (~15 nm) by adjusting the experimental conditions. The prepared MNP were functionalized with silica-based compounds (tetraethyl orthosilicate and (3-Aminopropyl) triethoxysilane) to adjust the material surface charge from negative to positive for the removal of Cr(VI) in aqueous solution, as shown in Scheme 1.

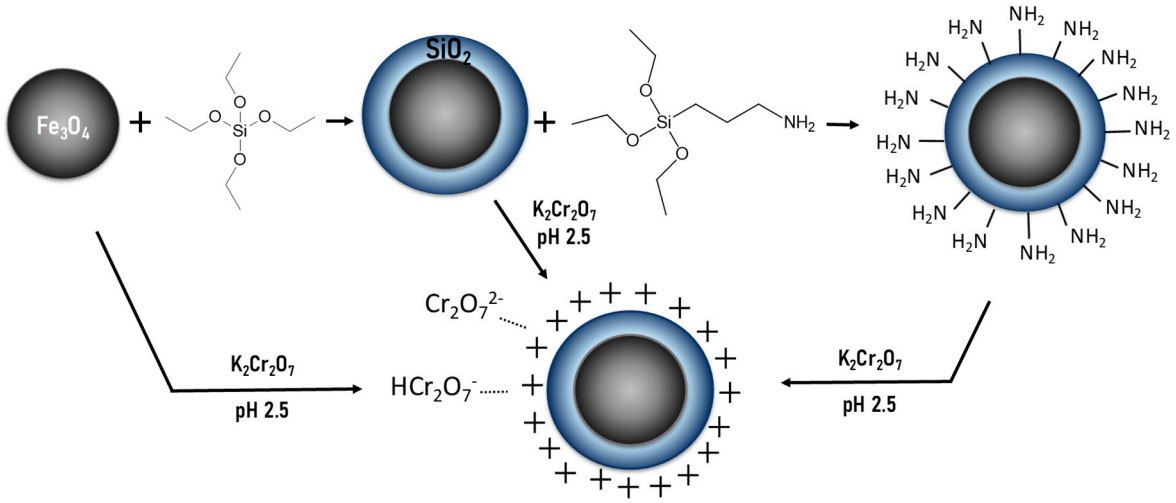

Scheme 1. Synthesis and functionalization of iron oxide magnetic nanoparticles with tetraethyl orthosilicate (TEOS) and (3-aminopropyl) triethoxysilane (APTES), and the adsorption strategy of Cr(VI). Adsorption experiments are conducted at pH 2.5, where all particles are positively charged and Cr species ($HCr_2O_7^-$ and $Cr_2O_7^{2-}$) are negatively charged.

2. Materials and Methods

2.1. Chemical Reagents and Analysis

Iron(II) acetate (≥98%), diethylene glycol (DEG, ≥99%), 2-propanol (≥99%), tetraethyl orthosilicate (TEOS, ≥99%), ammonium hydroxide (30%), (3-Aminopropyl) triethoxysilane (APTES, 99%), ethanol (≥99.8%), nitric acid (HNO_3, 65%) and methanol (≥99%) were purchased from Sigma-Aldrich, Madrid,

Spain. A total of 500 mg/L stock solution of Cr(VI) was prepared by dissolving a specific amount of potassium dichromate in 500 mL of distilled water. Working standards of desired Cr(VI) concentrations were prepared by diluting different volumes of the stock solution. The Cr(VI) concentration was estimated by inductively coupled plasma optical emission spectroscopy (ICP-OES) with an apparatus from Perkin Elmer, model OPTIME 2100DV, Akron, Ohio, U.S., considering a wavelength of 540 nm.

2.2. Magnetic Nanosorbent Preparation

The synthesis of the iron oxide magnetic nanoparticles was carried out using a microwave oven Monowave 300 produced by Anton Paar GmbH, Austria, working at 2.45 GHz and equipped with a built-in magnetic stirrer, a temperature controller by an internal fiber-optics probe, an infrared sensor for surface temperature and a pressure meter. A mixture containing 0.3 g of iron(II) acetate, 18.3 mL of DEG and 0.7 mL of distilled water was placed into the microwave reactor and stirred at 600 rpm, while the temperature increased at a rate of 3.75 °C/min until 170 °C. The mixture was left for 2 h at that temperature. Finally, the obtained product was collected and washed several times with ethanol by centrifugation at a relative centrifugal force (RCF) of 8000 for 15 min and suspended in 2-propanol for further functionalization and in water for the sorption process.

The MNP were grafted with a layer of silica (TEOS@MNP) by using the Stöber process, in which a mixture of 100 mg of MNP, 200 mL of 2-propanol and 100 mL of distilled water was sonicated for 15 min at 20 °C. Then, 20 mL of ammonium hydroxide was added to the mixture and, while sonicating, TEOS was added dropwise and the mixture was left under sonication for another 15 min. The sample was then collected by centrifugation at 8000 RCF for 45 min, washed several times with ethanol and then suspended in 2-propanol for the APTES functionalization and in water for the adsorption process.

A second grafting with APTES was performed over the TEOS@MNP, where an aliquot of the dispersion containing 50 mg of the material was taken to 20 mL 2-propanol and then sonicated for 5 min. Afterwards, while sonicating, 0.5 mL of APTES was added dropwise and left sonicating for 1 h. The final sample was washed with ethanol and collected by centrifugation at 8000 RCF/g for 15 min.

2.3. Characterization

The material crystalline structure was analyzed by X-ray diffraction (XRD) with a Bruker D8 Advance diffractometer with a graphite monochromator using CuKα radiation (λ = 1.5406 Å), within 10 and 70 2θ degrees. The crystal size was calculated by using Rietveld refinement [22]. On the other hand, the particle size and morphology were determined by transmission electron microscopy (TEM) using a JEOL JEM 1010 microscope (Pleasanton, CA, USA) operated at 100 keV, and the mean particle size was obtained by measuring the largest internal width of at least 200 particles. For TEM observation, samples were prepared by diluting the suspension and placing one drop of it on an amorphous carbon-coated copper grid.

The colloidal properties of the MNP were studied by dynamic light scattering in a Malvern Instrument Zetasizer Nano SZ (Malvern, UK) equipped with a solid-state He-Ne laser (λ = 633 nm). The hydrodynamic particle size of the samples was obtained at pH 2.5 in a standard cuvette and with a refraction index of 2.42. The hydrodynamic size was evaluated as the mean value of the distribution by number. Also, zeta potential measurements were performed to determine the nanoparticle surface charge as a function of pH at room temperature by varying the pH of the suspensions between 2 and 12, using HNO_3 and KOH and using 10^{-2} M KNO_3 as electrolyte.

A vibrating sample magnetometer—MagLabVSM, Oxford Instrument (High Wycombe, UK)—was used to measure the magnetic properties of the MNP before and after grafting, where the samples were accurately weighted and pressed into a sample holder. The hysteresis loops of the powder samples were measured at 290 K up to 3000 kA/m, and the magnetic saturation of the material was obtained by extrapolating to 1/H = 0 the high field part of the magnetization curve.

Fourier transform infrared spectra (FTIR) were performed to confirm the presence of the silica shell and APTES grafting on the magnetic nanoparticle surface. For this, dried powder samples were

diluted in KBr at 2% w/w, pressed into pellets and measured in Bruker IFS 66VS (Billerica, MA, USA) apparatus in the range of 400–4000 cm^{-1}.

2.4. Kinetic Measurements

Kinetic experimentation was performed at a pH of 2.5 and initial Cr(VI) concentration of 20 mg_{Cr}/L by varying the adsorption time (5, 15, 30, 45, 60, 90, 120 and 1440 min). After each adsorption experiment, the magnetic nanosorbent was separated by using a 60 × 30 mm magnet with a field at the surface of 320 kA/m. The residual Cr(VI) concentration in the supernatant was measured by ICP-OES. The experimental data were analyzed with three different kinetic models: pseudo-first-order (PFO), pseudo-second-order (PSO) and Elovich.

PFO is considered to describe the adsorption initial stage with long adsorption times and a system almost in equilibrium well. The non-linear form of the PFO rate equation is given by Equation (1) [23]:

$$q_t = q_e\ (1 - e^{-kt}) \quad (1)$$

where t is the contact time in min, k_1 the first order adsorption rate constant in min^{-1}, q_e is the equilibrium adsorption capacity in mg/g, and q_t the adsorption capacity at contact time t in mg/g.

The PSO model is used to explain processes ruled by the surface adsorption, as well as most environmental processes [24]. This model also indicates that the adsorption is due to physicochemical interactions between the adsorbate and adsorbent [25]. The second-order adsorption rate constant in g/mg (k_2) was obtained from the non-linear equation described in Equation (2) [26]:

$$q_t = k_2 {q_e}^2 t/(1 + k_2 q_e t) \quad (2)$$

In contrast, the Elovich model fits adsorption processes far from equilibrium well and with a mechanism of chemisorption for long periods of time, neglecting the desorption process. The non-linear form of the Elovich rate equation is given by Equation (3) [23]:

$$q_t = (1/\beta)\ \ln(\alpha\beta t) \quad (3)$$

where β is a desorption constant related to the extent of surface coverage and activation energy for chemisorption, and α is the initial adsorption rate in mg/g min.

2.5. Sorption Experimentation

Batch Cr(VI) adsorption experiments were carried out at room temperature (20 °C) in a plastic 15 mL conical vial containing 5 mg of the nanosorbent (MNP, TEOS@MNP and APTES@TEOS@MNP) and 10 mL of Cr(VI) solutions with different initial concentrations (from 10 to 100 mg/L) selected to avoid the complete elimination of chromium for measurement purposes and to reach adsorption equilibrium. The mixture was then mechanically mixed for 2 h and, after equilibrium, the MNP was collected in 1 minute using a 60 × 30 mm magnet with a field at the surface of 320 kA/m. The residual pollutant concentration in the supernatant (C_e, mg/L) in the aqueous phase was determined, and the adsorption capacity was calculated by Equation (4).

$$q_e = (C_0 - C_e)V/m \quad (4)$$

where q_e is the adsorption capacity equilibrium, in mg_{Cr}/g; C_0 is the initial Cr(VI) concentration, in mg/L; C_e is the equilibrium concentration, in mg/L; m is the dry weight of adsorbent, in g; and V is the volume of Cr(VI) solution, in L. The percentage of removal was obtained by Equation (5) [27]:

$$\text{Removal} = (C_0 - C_e)100/C_0 \quad (5)$$

The effect of the pH was analyzed in a pH range between 2 and 6 at a Cr(VI) initial concentration of 40 mg_{Cr}/L. The effect of initial concentration was studied by using 0, 10, 20, 30, 40, 50, 60, 70, 80, 90 and 100 mg_{Cr}/L in the experiments at optimum pH (2.5). The obtained experimental data were fitted to three different isotherm models: Langmuir, Freundlich and Temkin (Table 1). In each model, the dependence of the equilibrium adsorption capacity, q_e (mg/g) is stablished as a function of the pollutant equilibrium concentration, C_e (mg/L). The maximum adsorption capacity q_m (mg/g) was obtained by the Langmuir equilibrium model.

Table 1. Isotherm models linear equations and plots.

Isotherm	Linearized Equation	Plot
Langmuir	$C_e/q_e = 1/b_0q_m + C_e/q_m$	C_e/q_e vs. C_e
Freundlich	$lnq_e = lnK_f + (lnC_e)/n$	lnq_e vs. lnC_e
Temkin	$q_e = (RT/b_T)lnK_T + (RT/b_T)lnC_e$	q_t vs. lnC_e

The Langmuir isotherm model is considered to adjust well to processes in which the adsorbent presents a homogeneous surface and the adsorption is performed with monolayer coverage. In contrast, the Freundlich model describes adsorptions with non-existing limited levels and systems with heterogeneous surfaces, while the Temkin model considers that the adsorption heat reaction (b_T, J/mol) decreases in a linear way [28]. In each model, the dependence of the equilibrium adsorption capacity q_e (mg/g_{NS}) is taken as a function of the pollutant equilibrium concentration, Ce (mg/L).

Finally, the reusability of the nanosorbent after the Cr(VI) removal process was determined by analyzing the adsorption capacity of seven successive sorption/desorption cycles. For this, 20 mg was mechanically mixed at 60 rpm for 2 h with 40 mL of Cr(VI) solution 100 mg/L at pH 2.5. The Cr(VI)-loaded material was collected by magnetic harvesting after the sorption process and washed several times with distilled water. Then, 5 mL of NaOH, 0.01 M was added and mixed for 1 h at 20 °C. Finally, the nanosorbent was dried in an inox-coated oven at 50 °C overnight, and the procedure was repeated for each successive cycle.

3. Results and Discussion

3.1. Characterization

The MNP were synthesized by a microwave-assisted method that presents greater efficiencies in comparison with other approaches such as thermal decomposition with conventional heating. One of the most noticeable differences between these methods is that a microwave produces an internal homogenous heating that promotes the nucleation in the whole vessel at the same time, reducing the growth possibilities of the nuclei generated and consequently obtaining uniform particles of lower sizes [21]. The MNP TEM images are shown in Figure 1a, and the particle size distribution in Figure 1e. The particle size distribution was evaluated and adjusted to a log normal distribution in which a mean particle size of 12.2 (±1.5) nm was obtained. Moreover, the XRD pattern of the MNP was obtained and is displayed in Figure 1d, in which it can be seen that there was no extra reflection of other iron oxide phases such as hematite or iron hydroxides. The depicted reflections fit well with the space group (Fd-3m:227) typically assigned to cubic spinel structures. The crystallite size was calculated to be 12.8 (±0.3) nm by Rietveld refinement. It is worthwhile to mention that microwave-assisted synthesis increases the reproducibility of the sample.

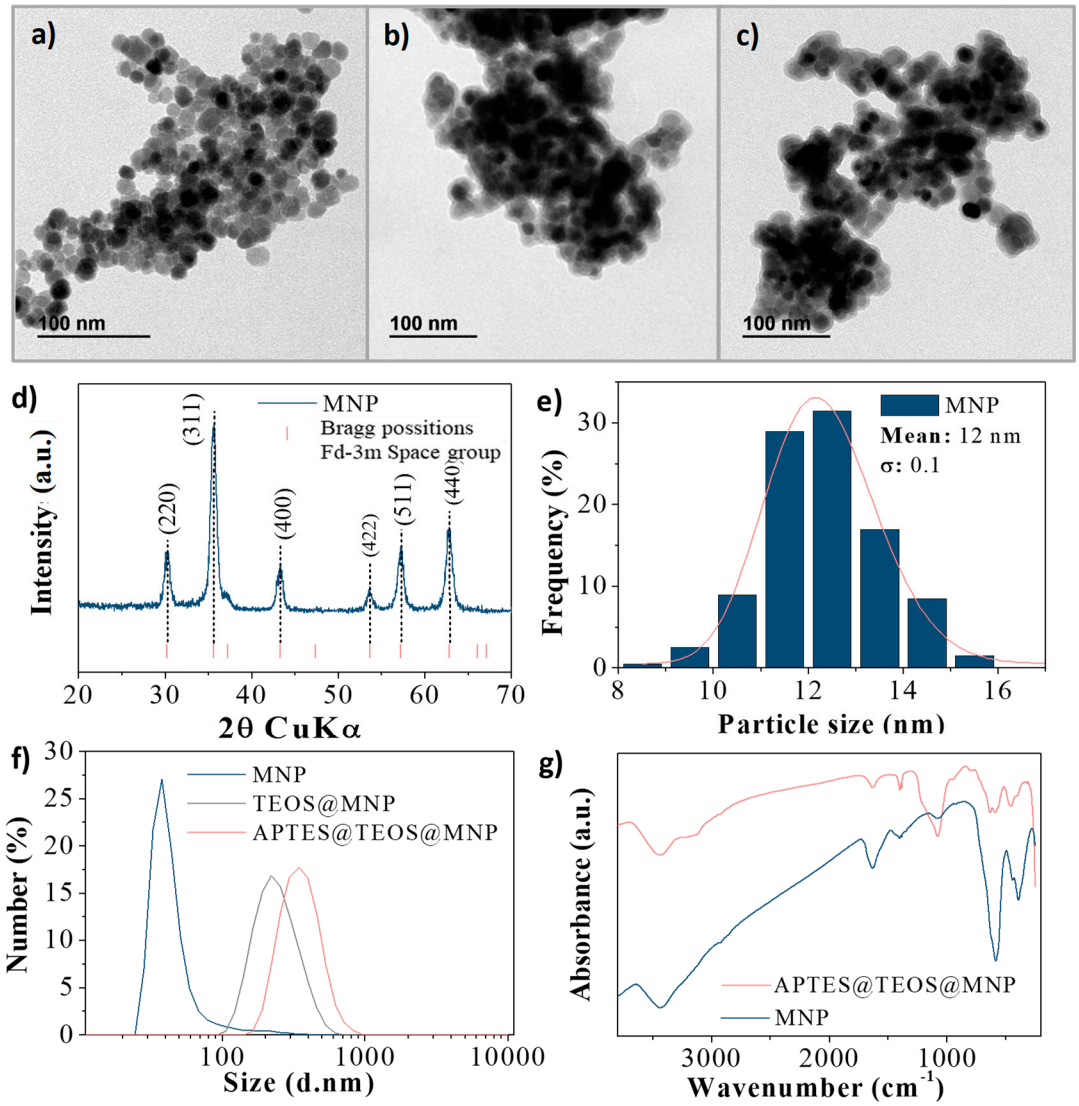

Figure 1. Morphological and structural characterization of the magnetic nanoparticles (MNP) before and after grafting: (**a**–**c**) transmission electron microscope (TEM) images of nanosorbents (**a**) MNP, (**b**) TEOS@MNP and (**c**) APTES@TEOS@MNP, (**d**) X-ray diffraction of the MNP, (**e**) MNP particle size distribution, (**f**) hydrodynamic size, and (**g**) Fourier transform infrared (FTIR) spectra. (a.u. corresponds to arbitrary units).

Figure 1b,c show the TEM images of the TEOS@MNP and APTES@TEOS@MNP, respectively. It can be seen that a smooth silica layer has been placed over the MNP agglomerates in both cases, indicating that the grafting was performed correctly. Figure 1f shows the hydrodynamic size distribution of the grafted and non-grafted particles. The mean sizes for the number distribution obtained for the MNP, TEOS@MNP and APTES@TEOS@MNP were 172.2(0.2) nm, 278.0(0.2) nm and 491.5(0.2) nm, respectively, indicating that the grafting enlarges the hydrodynamic particle size. Also, in the case of the MNP, the presence of a small fraction of bigger particles can be observed, suggesting that, without the silica layer, the particles form large aggregates.

To ascertain the presence of both graftings, FTIR analysis was performed and is shown in Figure 1g. It can be observed that the sample APTES@TEOS@MNP presents a band at approximately 1080 cm^{-1} which corresponds to the Si–O bond on the nanoparticles surface due to the silica grafting [28]. Also, the presence of coordinated –OH groups on the surface of the particles or water molecules with the unsaturated surface Fe atoms can be attributed to the bands at 3443 cm^{-1} and 1600 cm^{-1} of O–H

stretching vibration and O–H deformed vibration (bending modes), respectively [29]. The band at 468 cm^{-1} in both samples could be due to the Fe–O bonds of magnetite or maghemite [30]. The N–H bending and stretching bands of the terminal primary amine group of APTES cannot be seen as they overlapped with the 3443 cm^{-1} band; however, the grafting can be confirmed by the 2852 and 2932 cm^{-1} bands of the C–H bond stretching vibration that correspond to the propyl group [31]. Further confirmation of the presence of the APTES was obtained by the increase of surface charge of the particles and the displacement of the isoelectric point, as explained in the following section (Section 3.2).

Figure 2 shows the magnetization curves of the nanosorbents at room temperature. As can be observed, the remanence magnetization and the coercive field were nearly zero for all samples, indicating a superparamagnetic behavior at room temperature. The saturation magnetization values decrease after each grafting process from 81 to 62 and 58 Am^2/kg for the MNP, TEOS@MNP and APTES@TEOS@MNP, respectively, due to the addition of a non-magnetic material; i.e., around 23% in weight of TEOS plus 5% of APTES. Bare particles present a saturation magnetization close to the bulk value for magnetic iron oxides.

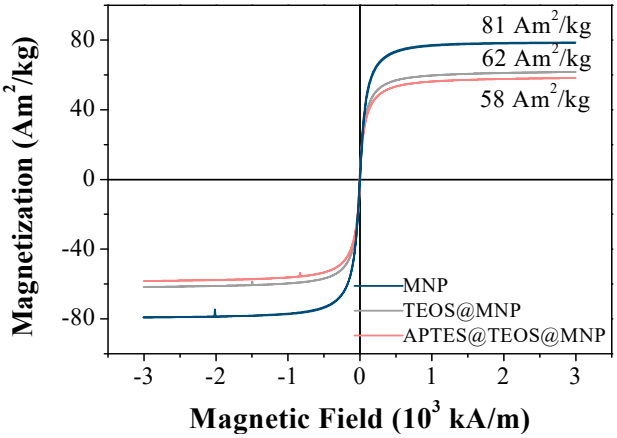

Figure 2. Magnetization curves of MNP before and after grafting with each magnetic saturation value in Am^2/kg of sample.

3.2. Adsorptive Measurements

3.2.1. Effect of pH

The effect of pH in the adsorption process of Cr(VI) was evaluated by using the non-grafted MNP in batch experimentation, in which the pH was varied between 2 and 6. It can be seen from Figure 3a that, after the adsorption process at different pH values, the obtained q_e values and Cr(VI) removal decrease with the increasing pH, which agrees with other studies on Cr(VI) adsorption with iron oxide nanoparticles [32,33]. This behavior can be attributed to the surface charge of the particles, as can be seen in Figure 3b. At low pH values, the MNP present a positive charge (+25.9 mV at pH 2.5) that increases the affinity of the nanosorbent for the anionic chromates ($Cr_2O_7^{2-}$ and $HCrO^{4-}$) in the aqueous solution. It should be taken into account that TEOS@MNP and APTES@TEOS@MNP samples are also positively charged at that pH (+1.8 and +34.2 mV, respectively), which can also be used to confirm the FTIR results regarding the success in the coating process. On the contrary, at high pH values, the MNPs are negatively charged, causing electrostatic repulsion for Cr(VI) anions [34]. Therefore, for further adsorption analyses and for the sake of comparison, a pH of 2.5 was fixed for the following experiments. The isoelectric point or point of zero charge of APTES@TEOS@MNP (pH 10) confirms the success of the coating process in comparison with the bare nanoparticles (pH 6.5). This huge difference is attributed to the presence of amino groups on the surface of the functionalized nanoparticles.

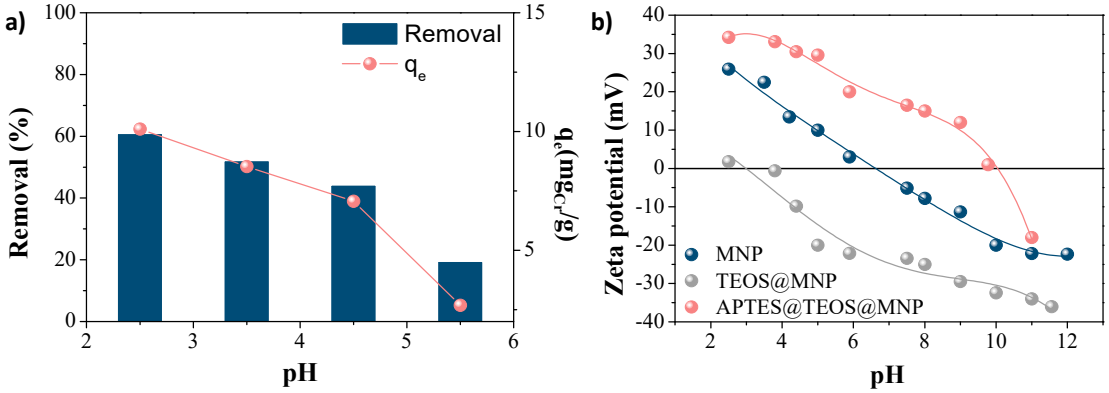

Figure 3. (**a**) Effect of the pH on the removal (%) and adsorption capacity (mg/g) of Cr(VI) with MNP. (**b**) Zeta potential curves of MNP, TEOS@MNP and APTES@TEOS@MNP.

3.2.2. Kinetics and Isotherms Models

The adsorption kinetics were analyzed for the three nanosorbents (MNP, TEOS@MNP and APTES@TEOS@MNP), and the non-linear fitting of the experimental data and kinetic models as a function of time are presented in Figure 4a. As can be seen, the adsorption equilibrium is reached after 1 h, and the experimental data best fitted the PSO model (R^2 = 0.98(0.02)), indicating that the rate-limiting step is the surface adsorption, and chemisorption is the most likely mechanism of adsorption [35]. Also, due to the surface charge, it is important to acknowledge that the mechanism of adsorption may benefit from the ion exchange between the Cr(VI) molecules, with the adsorbent TEOS@MNP barely removing the Cr(VI) of the aqueous solution due to its low surface charge.

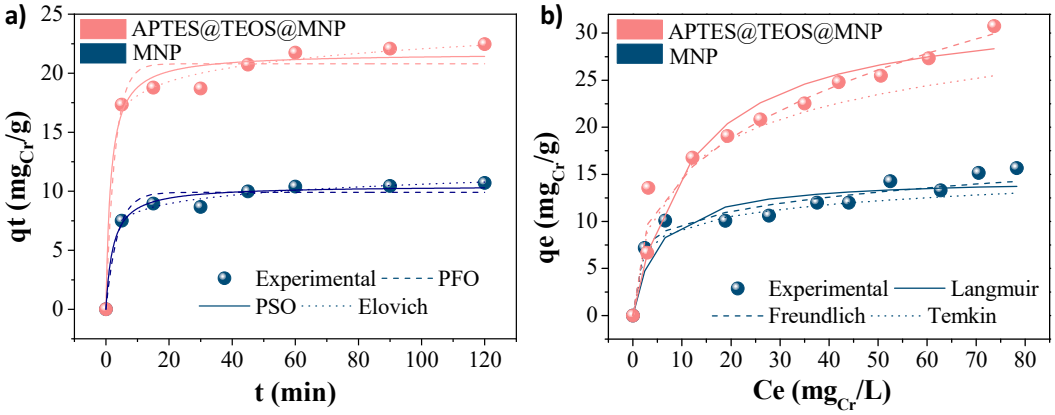

Figure 4. Adsorptive results of MNP and APTES@TEOS@MNP for Cr(VI) removal. (**a**) Non-linear kinetic models and (**b**) adsorption isotherms.

In contrast, the experimental data obtained by analyzing the effect of the initial concentration of Cr(VI) were compared to the previously mentioned isotherm models, and the corresponding non-linear fittings are included in Figure 4b. As can be seen, there was a better fitting with the Langmuir isotherm model in all cases ($R^2 \approx 0.98(0.02)$), meaning that it can be assumed that the process follows a monolayer adsorption with specific active sites for each Cr(VI) molecule. Furthermore, when using the APTES@TEOS@MNP, the maximum adsorption capacity obtained was higher (35 mg/g) than the obtained with the non-grafted MNP (15 mg/g), supporting the fact that the affinity of the nanosorbent increases with the surface charge. Table 2 summarizes the kinetic and isotherm parameters obtained with the experimental data.

Table 2. Kinetic and isotherm parameters.

Langmuir			Freundlich			Temkin		
Constant	**MNP**	**APTES**	**Constant**	**MNP**	**APTES**	**Constant**	**MNP**	**APTES**
b_0 (L/mg)	0.19	0.08	K_f (mg/g)/(L/g)1/n	6.32	6.55	b_t (J/mol)	1259.37	440.05
q_m (mg/g)	15.00	35.00	1/n	0.19	0.35	k_t (L/g)	17.38	1.90
R^2	0.98	0.97	R^2	0.88	0.84	R^2	0.85	0.93
Pseudo-First Order			**Pseudo-Second Order**			**Elovich**		
Constant	**MNP**	**APTES**	**Constant**	**MNP**	**APTES**	**Constant**	**MNP**	**APTES**
q_e (mg/g)	9.9	20.8	q_e (mg/g)	10.5	21.7	β (mg/g)	0.98	0.58
k_1	0.27	0.35	k_2	0.04	0.03	α (mg/g.min)	325	6445
R^2	0.96	0.95	R_2	0.98	0.98	R^2	0.89	0.88

3.2.3. Reusability Assays

Figure 5 shows the efficiency of the Cr(VI) adsorption with MNP and APTES@TEOS@MNP after seven adsorption/desorption cycles. These tests showed that Cr(VI)-loaded nanosorbent requires just a small volume of a basic solution to efficiently desorb the chromate molecules due to the change of the particles' surface charge with pH. In both cases, only a slight decrease of efficiency was shown (≈98 ± 5%), proving that the nanosorbents are reusable and highly efficient in this adsorption process. Even though the maximum adsorption capacities obtained for MNP and APTES@TEOS@MNP were not as good as for other functionalized magnetic nanoparticles (Table 3), this material can be used several times and achieve greater chromium removals. Also, after seven cycles, there was no change in the morphology of the nanosorbents as demonstrated with TEM images, and there was no magnetic loss observed (95% recovery).

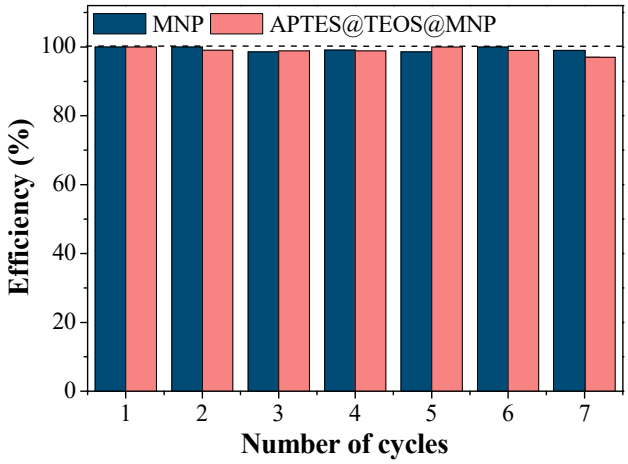

Figure 5. MNP and APTES@TEOS@MNP reusability tests for seven consecutive adsorption/desorption cycles.

In a previous work [15], we obtained lower q_m (12 mg/g) values with bare nanoparticles synthetized via an electrochemical method with a mean particle size of 21 nm. In the present work, we have improved the adsorption efficiency by reducing the nanoparticle size to 12 nm, obtaining a q_m value of 15 mg/g for bare NPs. Table 2 presents a comparison of the adsorption capacity of Cr(VI) by using different magnetic nanosorbents with similar characteristics to the one used in this work. As can be seen for Cr(VI) removal, it is important to ensure a positive surface charge of the adsorbent at the working pH to reinforce attraction forces with negatively charged chromates. Additionally, the maximum adsorption capacity of Cr(VI) (q_m = 35 mg/g) makes our APTES@TEOS@MNP a competitive adsorbent compared to other materials. Only the chitosan-coated Fe_3O_4 nanocomposite shows a high q_m (81.5 mg/g), which is probably due to the quelate effect of the chitosan with the chromates,

enhancing the adsorption efficiencies, but this may hinder its re-use, unlike the material presented in this research which can be used for several adsorption cycles, reaching higher removal percentages and lowering the process cost. In general, we have observed that the adsorption capacity increases by increasing the nanoparticle surface charge, as in the case from +1.8 mV (q_m = 0 mg/g for TEOS@MNP) to +34.2 mV (q_m = 35 mg/g for APTES@TEOS@MNP).

Table 3. Maximum adsorption capacities (q_m, mg/g) of Cr(VI) for different nanosorbents. (PAA = Polyacrylic acid, MPA = Mercaptopropionic acid).

Adsorbent	Surface Charge	pH (-)	q_m (mg/g)	Reference
TEOS@MNP	Slightly positive	2.5	0	This work
Fe_3O_4@n–SiO_2 NPs	Slightly positive	2	3.8	[33]
Fe_3O_4 (PAA-coated and amino-functionalized)	Negative	3	11.2	[36]
Diatomite-supported magnetite NPs	Positive	2	11.4	[34]
Iron oxide magnetic nanoparticles (MNPs)	Positive	2.5	15	This work
Maghemite nanoparticles	Positive	2.5	17	[37]
APTES@TEOS@MNP	Positive	2.5	35	This work
(3-MPA)-functionalized iron oxide NPs	Positive	1	45	[38]
Chitosan-coated Fe_3O_4 nanocomposites	Positive	2	81.5	[32]

4. Conclusions

Superparamagnetic nanosorbents based on iron oxide nanoparticles of 12.2 (±1.5) nm in diameter and coated by silica (30% in weight) were developed and optimized for the removal of Cr(VI). It was observed that surface charge is an important parameter determining the adsorption capacity, reaching a maximum of 35 mg Cr(VI) per g of nanosorbent at the maximum positive surface charge.

In this work, microwave polyol-mediated synthesis was chosen for the efficient and reproducible preparation of uniform magnetic cores with sizes below 15 nm to maintain superparamagnetic behavior, and the surface charge was varied from negative to positive by successively grafting tetraethyl orthosilicate and 3-Aminopropyl triethoxysilane. Chromium surface adsorption seems to be the rate-limiting step, and adsorption increases with increasing the nanoparticles' positive surface charge. Finally, the particles showed high reusability efficiencies (around 100%) after seven Cr(VI) desorption cycles.

The easy separation and regeneration of these magnetic nanosorbents from aqueous solutions, and the high-adsorption capacity of Cr(VI) in comparison to others, suggest that these nanoparticles can be efficiently used for the decontamination of Cr(VI)-containing wastewater, such as that discharged by the electroplating industry.

Author Contributions: Conceptualization, A.G.-C. and E.M.; Data curation, A.G.-C.; Formal analysis, A.G.-C. and E.M.; Funding acquisition, M.d.P.M. and E.M.; Investigation, A.G.-C. and E.M.; A.G.-C. and E.M.; Project administration, M.d.P.M.; Resources, M.d.P.M. and E.M.; Software, M.d.P.M.; Supervision, M.d.P.M. and E.M.; Validation, A.G.-C. and E.M.; Visualization, M.d.P.M.; Writing—original draft, A.G.-C.; Writing—review and editing, A.G.-C., M.d.P.M. and E.M.

Funding: This research was funded by the Spanish Ministry of Economy and Competitiveness under grants MAT2017-88148-R, PGC2018-095642-B-I00 and Juan de la Cierva Formación FJCI-2015-23702.

Conflicts of Interest: There are no conflict to declare.

References

1. Carolin, C.F.; Kumar, P.S.; Saravanan, A.; Joshiba, G.J.; Naushad, M. Efficient techniques for the removal of toxic heavy metals from aquatic environment: A review. *J. Environ. Chem. Eng.* **2017**, *5*, 2782–2799. [CrossRef]
2. Bhattacharya, S.; Gupta, A.B.; Gupta, A.; Pandey, A. Introduction to Water Remediation: Importance and Methods. In *Water Remediation*; Springer: Singapore, 2018; pp. 3–8. [CrossRef]

3. Burakov, A.E.; Galunin, E.V.; Burakova, I.V.; Kucherova, A.E.; Agarwal, S.; Tkachev, A.G.; Gupta, V.K. Adsorption of heavy metals on conventional and nanostructured materials for wastewater treatment purposes: A review. *Ecotoxicol. Environ. Saf.* **2018**, *148*, 702–712. [CrossRef] [PubMed]
4. Barakat, M.A. New trends in removing heavy metals from industrial wastewater. *Arab. J. Chem.* **2011**, *4*, 361–377. [CrossRef]
5. Almeida, J.C.; Cardoso, C.E.D.; Tavares, D.S.; Freitas, R.; Trindade, T.; Vale, C.; Pereira, E. Chromium removal from contaminated waters using nanomaterials—A review. *TrAC Trends Anal. Chem.* **2019**, *118*, 277–291. [CrossRef]
6. Gheju, M. Progress in Understanding the Mechanism of CrVI Removal in Fe0-Based Filtration Systems. *Water* **2018**, *10*, 651. [CrossRef]
7. Abbas, A.; Al-Amer, A.M.; Laoui, T.; Al-Marri, M.J.; Nasser, M.S.; Khraisheh, M.; Atieh, M.A. Heavy metal removal from aqueous solution by advanced carbon nanotubes: Critical review of adsorption applications. *Sep. Purif. Technol.* **2016**, *157*, 141–161. [CrossRef]
8. Owlad, M.; Aroua, M.K.; Daud, W.A.W.; Baroutian, S. Removal of Hexavalent Chromium-Contaminated Water and Wastewater: A Review. *Water Air Soil Pollut.* **2008**, *200*, 59–77. [CrossRef]
9. Bolisetty, S.; Peydayesh, M.; Mezzenga, R. Sustainable technologies for water purification from heavy metals: Review and analysis. *Chem. Soc. Rev.* **2019**, *48*, 463–487. [CrossRef]
10. Barrera-Diaz, C.E.; Lugo-Lugo, V.; Bilyeu, B. A review of chemical, electrochemical and biological methods for aqueous Cr(VI) reduction. *J. Hazard. Mater.* **2012**, *223–224*, 1–12. [CrossRef]
11. Corral-Bobadilla, M.; González-Marcos, A.; Vergara-González, E.; Alba-Elías, F. Bioremediation of Waste Water to Remove Heavy Metals Using the Spent Mushroom Substrate of Agaricus bisporus. *Water* **2019**, *11*, 454. [CrossRef]
12. Kumari, M.; Pittman, C.U., Jr.; Mohan, D. Heavy metals [chromium (VI) and lead (II)] removal from water using mesoporous magnetite (Fe3O4) nanospheres. *J. Colloid Interface Sci.* **2015**, *442*, 120–132. [CrossRef] [PubMed]
13. Dolgormaa, A.; Lv, C.-J.; Li, Y.; Yang, J.; Yang, J.-X.; Chen, P.; Wang, H.-P.; Huang, J. Adsorption of Cu(II) and Zn(II) Ions from Aqueous Solution by Gel/PVA-Modified Super-Paramagnetic Iron Oxide Nanoparticles. *Molecules* **2018**, *23*, 2982. [CrossRef] [PubMed]
14. Simeonidis, K.; Mourdikoudis, S.; Kaprara, E.; Mitrakas, M.; Polavarapu, L. Inorganic engineered nanoparticles in drinking water treatment: A critical review. *Environ. Sci. Water Res. Technol.* **2016**, *2*, 43–70. [CrossRef]
15. Martínez, L.J.; Muñoz-Bonilla, A.; Mazario, E.; Recio, F.J.; Palomares, F.J.; Herrasti, P. Adsorption of chromium(VI) onto electrochemically obtained magnetite nanoparticles. *Int. J. Environ. Sci. Technol.* **2015**, *12*, 4017–4024. [CrossRef]
16. Zhu, N.; Ji, H.; Yu, P.; Niu, J.; Farooq, M.U.; Akram, M.W.; Udego, I.O.; Li, H.; Niu, X. Surface Modification of Magnetic Iron Oxide Nanoparticles. *Nanomaterials* **2018**, *8*, 810. [CrossRef]
17. Li, X.; He, Y.; Sui, H.; He, L. One-Step Fabrication of Dual Responsive Lignin Coated Fe3O4 Nanoparticles for Efficient Removal of Cationic and Anionic Dyes. *Nanomaterials* **2018**, *8*, 162. [CrossRef]
18. Mahmoudi, M.; Sant, S.; Wang, B.; Laurent, S.; Sen, T. Superparamagnetic iron oxide nanoparticles (SPIONs): Development, surface modification and applications in chemotherapy. *Adv. Drug Deliv. Rev.* **2011**, *63*, 24–46. [CrossRef]
19. Blanco-Andujar, C.; Ortega, D.; Southern, P.; Pankhurst, Q.A.; Thanh, N.T. High performance multi-core iron oxide nanoparticles for magnetic hyperthermia: Microwave synthesis, and the role of core-to-core interactions. *Nanoscale* **2015**, *7*, 1768–1775. [CrossRef]
20. Lastovina, T.A.; Budnyk, A.P.; Kubrin, S.P.; Soldatov, A.V. Microwave-assisted synthesis of ultra-small iron oxide nanoparticles for biomedicine. *Mendeleev Commun.* **2018**, *28*, 167–169. [CrossRef]
21. Brollo, M.E.F.; Veintemillas-Verdaguer, S.; Salvan, C.M.; Morales, M.P. Key Parameters on the Microwave Assisted Synthesis of Magnetic Nanoparticles for MRI Contrast Agents. *Contrast Media Mol. Imaging* **2017**, *2017*, 8902424. [CrossRef]
22. McCusker, L.B.; Von Dreele, R.B.; Cox, D.E.; Louër, D.; Scardi, P. Rietveld refinement guidelines. *J. Appl. Cryst.* **1999**, *32*, 36–50. [CrossRef]
23. Tan, K.L.; Hameed, B.H. Insight into the adsorption kinetics models for the removal of contaminants from aqueous solutions. *J. Taiwan Inst. Chem. Eng.* **2017**, *74*, 25–48. [CrossRef]

24. Li, H.; Hou, R.; Chen, Y.; Chen, H. Removal of Hexavalent Chromium from Aqueous Solutions Using Sulfonated Peat. *Water* **2019**, *11*, 1980. [CrossRef]
25. Deng, R.-J.; Jin, C.-S.; Ren, B.-Z.; Hou, B.-L.; Hursthouse, A. The Potential for the Treatment of Antimony-Containing Wastewater by Iron-Based Adsorbents. *Water* **2017**, *9*, 794. [CrossRef]
26. Ho, Y.S. Review of second-order models for adsorption systems. *J. Hazard. Mater.* **2006**, *136*, 681–689. [CrossRef]
27. Gallo-Cordova, A.; Silva-Gordillo, M.d.M.; Muñoz, G.A.; Arboleda-Faini, X.; Almeida Streitwieser, D. Comparison of the adsorption capacity of organic compounds present in produced water with commercially obtained walnut shell and residual biomass. *J. Environ. Chem. Eng.* **2017**, *5*, 4041–4050. [CrossRef]
28. Arriortua, O.K.; Insausti, M.; Lezama, L.; Gil de Muro, I.; Garaio, E.; de la Fuente, J.M.; Fratila, R.M.; Morales, M.P.; Costa, R.; Eceiza, M.; et al. RGD-Functionalized Fe3O4 nanoparticles for magnetic hyperthermia. *Colloids Surf. B Biointerfaces* **2018**, *165*, 315–324. [CrossRef]
29. Iyengar, S.J.; Joy, M.; Ghosh, C.K.; Dey, S.; Kotnala, R.K.; Ghosh, S. Magnetic, X-ray and Mössbauer studies on magnetite/maghemite core–shell nanostructures fabricated through an aqueous route. *RSC Adv.* **2014**, *4*, 64919–64929. [CrossRef]
30. Medina, R.P.; Nadres, E.T.; Ballesteros, F.C.; Rodrigues, D.F. Incorporation of graphene oxide into a chitosan–poly (acrylic acid) porous polymer nanocomposite for enhanced lead adsorption. *Environ. Sci. Nano* **2016**, *3*, 638–646. [CrossRef]
31. Sodipo, B.K.; Aziz, A.A. A sonochemical approach to the direct surface functionalization of superparamagnetic iron oxide nanoparticles with (3-aminopropyl) triethoxysilane. *Beilstein J. Nanotechnol.* **2014**, *5*, 1472–1476. [CrossRef]
32. Fang, X.B.; Fang, Z.Q.; Tsang, P.K.E.; Cheng, W.; Yan, X.M.; Zheng, L.C. Selective adsorption of Cr(VI) from aqueous solution by EDA-Fe3O4 nanoparticles prepared from steel pickling waste liquor. *Appl. Surf. Sci.* **2014**, *314*, 655–662. [CrossRef]
33. Srivastava, V.; Sharma, Y.C. Synthesis and Characterization of Fe3O4@n-SiO2 Nanoparticles from an Agrowaste Material and Its Application for the Removal of Cr(VI) from Aqueous Solutions. *Water Air Soil Pollut.* **2013**, *225*, 1776. [CrossRef]
34. Yuan, P.; Liu, D.; Fan, M.; Yang, D.; Zhu, R.; Ge, F.; Zhu, J.; He, H. Removal of hexavalent chromium [Cr(VI)] from aqueous solutions by the diatomite-supported/unsupported magnetite nanoparticles. *J. Hazard. Mater.* **2010**, *173*, 614–621. [CrossRef] [PubMed]
35. Obike, A.; Igwe, J.; Emeruwa, C.; Uwakwe, K.; Aghalibe, C. Diffusion-Chemisorption and Pseudo-Second Order Kinetic Models for Heavy Metal Removal from Aqueous Solutions Using Modified and Unmodified Oil Palm Fruit Fibre. *Chem. Sci. Int. J.* **2018**, *23*, 1–13. [CrossRef]
36. Zhao, Y.G.; Shen, H.Y.; Pan, S.D.; Hu, M.Q. Synthesis, characterization and properties of ethylenediamine-functionalized Fe3O4 magnetic polymers for removal of Cr(VI) in wastewater. *J. Hazard. Mater.* **2010**, *182*, 295–302. [CrossRef]
37. Hu, J.; Lo, I.; Chen, G. Performance and mechanism of chromate (VI) adsorption by δ-FeOOH-coated maghemite (γ-Fe2O3) nanoparticles. *Sep. Purif. Technol.* **2007**, *58*, 76–82. [CrossRef]
38. Burks, T.; Avila, M.; Akhtar, F.; Gothelid, M.; Lansaker, P.C.; Toprak, M.S.; Muhammed, M.; Uheida, A. Studies on the adsorption of chromium(VI) onto 3-Mercaptopropionic acid coated superparamagnetic iron oxide nanoparticles. *J. Colloid Interface Sci.* **2014**, *425*, 36–43. [CrossRef]